International Journal of Fatigue, Volume 122, May 2019, Pages 208-217
DOI:10.1016/j.ijfatigue.2019.01.017

Criticality of porosity defects on the fatigue performance of wire + arc additive manufactured titanium alloy

Romali Biswal[a], Xiang Zhang[a,*], Abdul Khadar Syed[a], Mustafa Awd[b], Jialuo Ding[c], Frank Walther[b], Stewart Williams[c]

[a] Research Centre for Manufacturing and Materials Engineering, Coventry University, Coventry, CV1 5FB, UK

[b] Department of Materials Test Engineering, TU Dortmund University, 44227 Dortmund, Germany

[c] Welding Engineering and Laser Processing Centre, Cranfield University, Cranfield, MK43 0AL, UK

[*] Corresponding author; Email addresses: biswalr@uni.coventry.ac.uk; xiang.zhang@coventry.ac.uk

Abstract

This study was aimed at investigating the effect of internal porosity on the fatigue strength of wire + arc additive manufactured titanium alloy (WAAM Ti-6Al-4V). Unlike similar titanium alloys built by the powder bed fusion processes, WAAM Ti-6Al-4V seldom contains gas pores. However, feedstock may get contaminated that may cause pores of considerable size in the built materials. Two types of specimens were tested: (1) control group without porosity referred to as reference specimens; (2) designed porosity group using contaminated wires to build the specimen gauge section, referred to as porosity specimens. Test results have shown that static strength of the two groups was comparable, but the elongation in porosity group was reduced by 60% and its fatigue strength was 33% lower than the control group. The stress intensity factor range of the crack initiating pore calculated by Murakami's approach has provided good correlation with the fatigue life. The kink point on the data fitting curve corresponds well with the threshold value of the stress intensity factor range found in the literature. For predicting the fatigue limit, a modified Kitagawa-Takahashi diagram was proposed consisting of three regions depending on porosity size. Critical pore diameter was found to be about 100 micrometres.

Keywords: Porosity defects, Stress intensity factor, Kitagawa-Takahashi diagram, Ti-6Al-4V, Additive manufacturing

1. Introduction

The additive manufacturing (AM) technology is a highly effective method to reduce the production time and cost comparing to the traditional manufacturing process, i.e. machining parts from forged billets. Compared to the powder based AM processes, the wire + arc additive manufacture (WAAM) has a much higher material deposition rate, lower process cost and no powder handling requirement. Consequently, WAAM has found applications in the aerospace and other industrial sectors [1,2]. In addition, WAAM is reported to deliver fully dense (>99.99%) Ti-6Al-4V components with virtually no defects [3].

One of the main challenges to the widespread use of AM technologies to produce safety critical structural components has been widely recognised as the issues of material properties and repeatability, in particular the fatigue and fracture properties. Investigations on AM Ti-6Al-4V have shown that the static strength, fatigue crack growth rate and fracture toughness properties of WAAM [4,5], laser powder

Published by Elsevier. This is the Author Accepted Manuscript issued with: Creative Commons Attribution Non-Commercial No Derivatives License (CC:BY:NC:ND 4.0).
The final published version (version of record) is available online at DOI:10.1016/j.ijfatigue.2019.01.017. Please refer to any applicable publisher terms of use.

bed fusion in stress relieved condition [6] and electron powder bed fusion [7] are all comparable with the traditional wrought counterparts. However, the high cycle fatigue strength was much lower in some AM Ti-6Al-4V, with large variations and scatter in the S-N data. The process-induced defects, such as gas pores and lack of fusion cracks, are reported to be the cause for the poor performance and data scatter [5–11].

Another cause for the test data scatter has been identified as the AM microstructure characteristics that are controlled by the cooling rate and peak temperature during deposition [12]. The volume fraction of α phase reported for WAAM Ti-6Al-4V is greater than 90% [13,14], with a predominantly Widmanstätten microstructure and an average α lath width of 1.5±1 μm [13–15]. The prior β grains are columnar and aligned in the build direction, which can lead to mechanical property anisotropy in terms of the tensile [5,16] and fatigue strength [5].

Although WAAM Ti-6Al-4V seldom contains process-induced defects, studies have shown that feedstock contamination can be a common source for occurrence of gas pores [5,17]. Recent advances on the application of in-situ rolling [18] and inter-pass rolling techniques [19,20] have shown promising results in homogenising the microstructure by making the prior β grains equiaxed and more importantly, eliminating the process-induced defects in the build stage. However, adding a processing step significantly increases the production time and cost.

In terms of modelling of defects and fatigue life prediction, there are three approaches in the literature, namely, statistical (such as the weakest link theory [21–24]), classic notch fatigue method treating porosity as a stress raiser [25–27], and fracture mechanics approach [9,28–33]. The statistical approaches discussed in [22–24] have been used effectively for correlating fatigue life with the initial distribution of porosity obtained from X-ray computed tomography. However, parts made of wire-based AM processes exhibit far fewer and isolated pores [5,34,35], hence the use of statistical approach may not be suitable. A study based on the notch fatigue method, which is implemented in the FEMFAT fatigue post-processor [27], reported better fatigue life prediction accuracy, using the average stress acting on a finite volume of material in the notch root that is subjected to stress level greater than 90% of the maximum stress. This method is yet to be applied to titanium alloys. The rest of literature studies on notch fatigue and fracture mechanics methods were focused on powder based AM processes due to the concerns of higher porosity density.

The Kitagawa-Takahashi diagram [36] has been one of the most used analysis tools for qualitative representation of the fatigue design limits. The two limits in the diagram are obtained from the material test results, i.e. the fatigue limit in defect-free condition taken from the S-N data and the threshold value of the stress intensity factor range, which gives the condition for non-propagating cracks [37]. However, short cracks grow much faster than that would be predicted by linear elastic fracture mechanics [38]. Therefore El Haddad et al. introduced a fictitious crack size to raise the crack driving force in the short crack regime [29]. Later, Murakami and Endo [39] proposed a parameter based on the projected area of defect to represent an effective crack size for embedded defects. Consequently, the El Haddad model [29] and the root area parameter were adapted by Beretta and Romano to determine the non-propagating

crack condition for the lack of fusion defects encountered in AM materials [30]. These approaches [29,30,36,39] have been proven to be accurate for the lack of fusion defects [9,32,40], which are similar to a planar crack geometry. However, only one study has tested Murakami's approach on gas pore defects and found it to be conservative [41].

This study aims to investigate the effect of gas pore defects on the fatigue performance of WAAM Ti-6Al-4V. The probability of feedstock contamination cannot be neglected, therefore, two groups of WAAM Ti-6Al-4V specimens were tested, (1) reference group, built according to the standard manufacturing procedure using clean wire and optimised processing parameters, and (2) porosity group, built with contaminated wires in specimen gauge section using the same process parameters as for the reference group, to represent the feedstock contamination. X-ray computed tomography was performed to determine the porosity morphology and density in both groups. Fatigue testing was performed followed by fracture surface analysis to determine the fatigue crack initiating pore. Fracture mechanics approach was used to correlate the test results and to determine the fatigue strength limit with the effect of porosities.

2. Experiment design

2.1 Manufacturing

WAAM Ti-6Al-4V walls were deposited using a HiVE machine (High-Value Engineering) which has a Fronius Plasma 10 module attached to a rotator, allowing the co-axial rotation of the shield, wire feeder and the wire spool around the plasma torch. Table 1 shows the chemical composition of the Ti-6Al-4V wire (AWS 5.16- grade 5, 1.2 mm diameter) and the walls deposited for the study. Chemical composition of the wire was taken from the product certificate and that of the deposited walls from energy dispersive X-ray spectroscopy (for the primary elements) and LECO® analysis (for gaseous elements). The base plate was a hot-rolled Ti-6Al-4V of 12 mm thickness and was clamped to a rigid steel backing block during deposition. The clamping of the base plate prevents any distortion due to thermal residual stresses. The plasma arc was controlled by a Fanuc robot arc mate 120i. Heat from the substrate was extracted by a water-cooled backing plate. Argon gas of 99.99% purity was used as shielding gas (placed ahead of the torch and as well as the trailing end of the torch), directed precisely at the melt pool to avoid oxidation. The material was deposited by the oscillation strategy as shown in Fig. 1(a), which resulted in a wall of 27 mm thickness as shown in Fig. 1(b).

Table 1. Chemical composition (weight %) of wire feedstock and deposited walls (reference and porosity). [NA: data not available].

	Al	V	Fe	O	C	N	H	Residual	Ti
Wire	6.24	4.18	0.131	0.15	0.013	0.009	0.005	<0.4	Balance
Reference wall	5.61	3.8	NA	0.18	NA	0.008	0.007	NA	NA
Porosity wall	5.89	3.8	NA	0.17	NA	0.017	0.006	NA	NA
Allowable [42] limits or max	5.5-6.75	3.5-4.5	0.3	0.2	0.08	0.05	0.015	<0.4	Balance

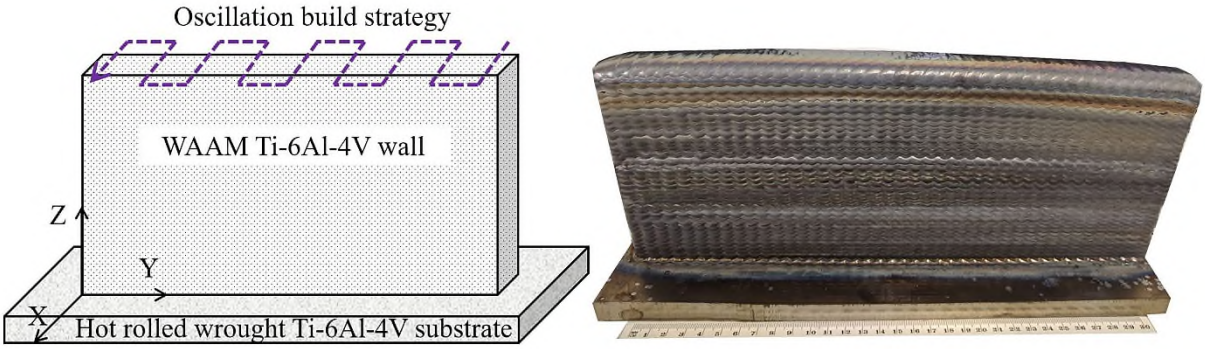

(a)
(b)

Fig. 1 (a) Schematic of WAAM Ti-6Al-4V wall deposition strategy, (b) a finished wall used for specimen extraction (material was deposited in *Z*-direction).

2.2 Specimens extraction and tests

Two walls, referred to as 'reference' and 'porosity', were built with optimised processing parameters. The reference wall was deposited entirely with clean wires as shown in Fig. 2(a), such that the specimens extracted from this wall should either be in defect free condition or contain pores of negligible size, which we refer to as micron sized pores; fatigue testing of specimens from the reference group should deliver the material intrinsic property. The so-called porosity wall was deposited using contaminated wires at the wall mid-section, which corresponded to the gauge section of the extracted specimens, and the rest of the porosity wall was built with clean wire as shown in Fig. 2(b). According to a previous study [5], pores of sizes over hundreds of microns can be caused due to feedstock contamination, which we refer to as macro pores. Wire contamination was done using water displacement 40th formula (WD-40®). Test specimens were extracted in parallel with the build direction.

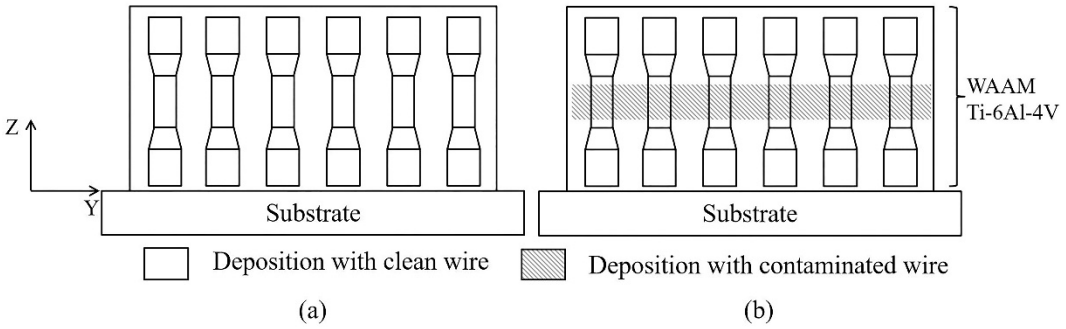

Fig. 2 Schematic of two walls and specimen extraction: (a) reference specimens (defect-free or scarce micron sized pores), (b) porosity specimens (pore sizes over hundreds of microns). Material was deposited in *Z*-direction.

Metallographic samples were prepared according to ASTM E3 standard [43] and etched using Kroll's reagent. Flat tensile specimens were machined according to ASTM E8 standard [44] as shown in Fig. 3(a), using wire electrical discharge machining (WEDM). Specimen surface roughness was measured with a light interferometer and was found to be 2±0.3 µm. Four specimens each from the reference and porosity group were tested under static tension load with a 250 kN Instron servo-hydraulic

test machine at room temperature at a cross-head speed of 1 mm/min. Strain was measured with an Instron extensometer of 25 mm gauge length.

Fatigue test specimens were machined according to ASTM E466 standard from the reference and porosity walls as shown in Figs. 3(b) and 3(c) respectively. The cylindrical specimens were polished at the gauge section with 600, 1200, 2500 and 4000 grit papers to achieve a final surface roughness of 0.5±0.1 μm. Fatigue tests were conducted with a 100 kN Instron servo-hydraulic test machine. Load controlled test was performed at a load ratio of 0.1 and frequency of 50 Hz, at laboratory room temperature condition.

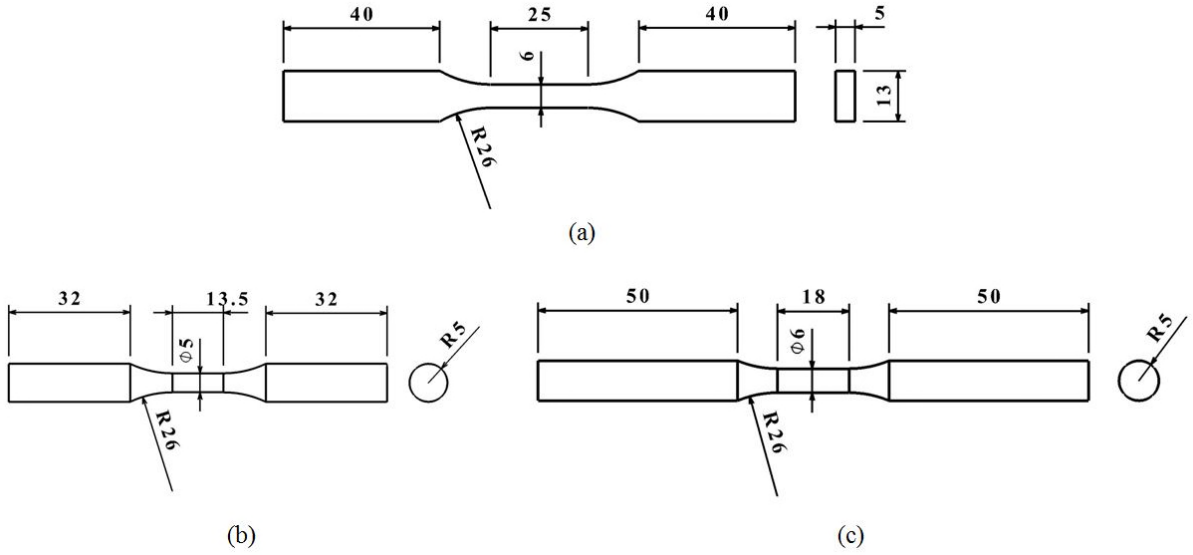

Fig. 3 Geometry and dimension of test specimens for (a) tensile tests, (b) and (c) load-controlled fatigue test from reference and porosity group respectively (unit: mm).

3 Experimental results and discussion

3.1 Microstructure analysis

Owing to the directional solidification, the prior β grains grow epitaxially in the build direction with lengths ranging from a few 100 microns to the entire height of the wall as shown in Fig. 4(a). The prior β grains are about 1~3 mm wide, which is much larger than the prior β grain width reported in the selective laser melting and electron beam melting processed Ti-6Al-4V [7,15,36].

Fig. 4(b) is the enlarged view of a prior β grain showing the variation in the α phase morphology at the prior β grain boundary (Fig. 4c), away from prior β grain boundary (Fig. 4d) and at the intersection of each layer with the next layer (Fig. 4e). According to [45], grain boundary α forms at the prior β grain boundary and there is a preferred orientation relationship between the grain boundary α and the adjacent β grain ($<0001>_{\alpha}$ parallel to $<110>_{\beta}$). Therefore, the preferred orientation relationship at the prior β grain boundary leads to the formation of lamellar α colonies of 20-30 μm width (measured by line intersection method according to ASTM E112). In Fig. 4(d) α phase exhibits a Widmanstätten microstructure away from prior β grain boundary, with an average α lath width of 3±0.7 μm. However, at localised regions such as the intersection between two layers (Fig. 4e), the average α lath width was reduced to 1±0.2 μm.

The reduction in the α lath width at the intersection can be attributed to the higher cooling rate during the deposition of each new layer [5].

3.2 Porosity characterisation

Optical micrographs of representative pores from the reference and porosity walls are shown in Fig. 5(a) and Fig. 5(b) respectively. Characteristic length is defined as the width of α colony [46], which is 20-30 µm for WAAM Ti-6Al-4V and according to [47], when the pore diameter is less than 8 times of the characteristic length, the micro-crack growth will be influenced by the surrounding microstructure. In case of pores larger than 8 times the characteristic length (as in the porosity specimens where the average pore diameter is 200 µm), the pore will behave like a notch and the gross mechanical properties can be used for fatigue life predictions. However, in the reference specimens, average porosity diameter (~60 µm) is within the characteristic length scale, therefore, local microstructure will dominate the crack initiation and initial crack growth phase.

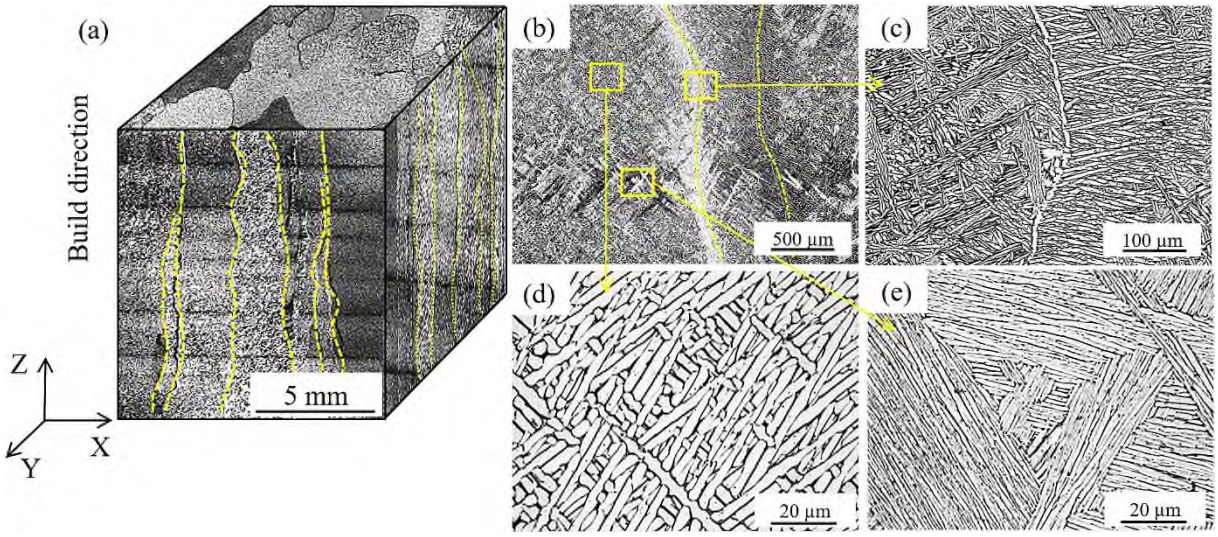

Fig. 4 Optical images showing: (a) macrostructure of as-deposited WAAM Ti-6Al-4V, (b) prior β grain boundary, with magnified views showing: (c) lamellar α colonies, (d) Widmanstätten microstructure, (e) fine lamellar α colonies indicated by darker bands between two layers.

X-ray CT analysis confirmed that the three-dimensional geometry of the pores was spherical in both reference and porosity specimens as shown in Fig. 5(c) and Fig. 5(d), which is in agreement with the results reported in ref. [48,49]. Density of the porosity specimens was found to be 99.96%, whereas the reference specimen density was more than 99.99% showing a fully dense material.

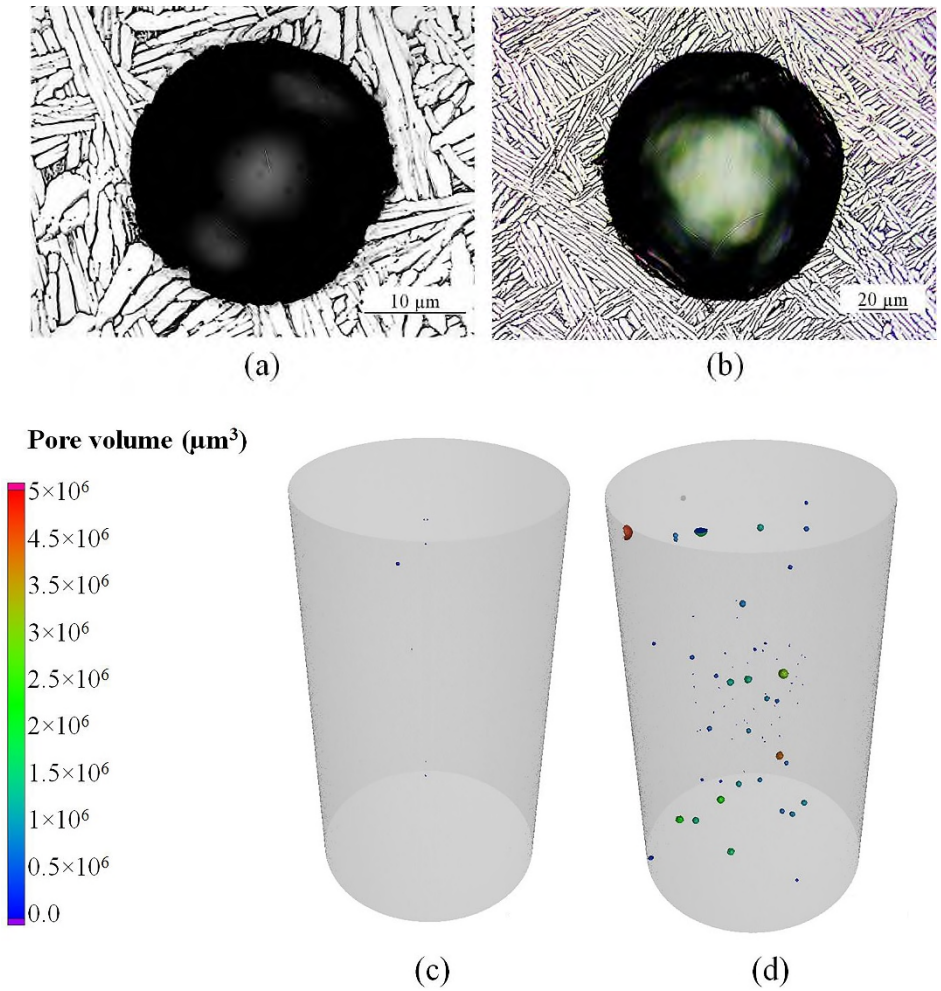

Fig. 5 Optical image of representative porosity in (a) reference wall, (b) porosity wall, comparing the size of the α lamellae width with the pore diameter (noting the different scales used), (c) X-ray computed tomography scan at specimen gauge section of the reference specimen, density is 99.99%, and (d) porosity specimen, density is 99.96%.

3.3 Tensile properties

The tensile test results for the reference and porosity specimens are shown in Fig. 6 and the property values are provided in Table 2. It is observed that the yield strength and ultimate tensile strength are comparable between the two groups. This is because that stress concentration at the pore has caused localised plastic deformation and the yield strength corresponds to the beginning of bulk material plastic deformation. After yielding the stress-strain curve becomes almost horizontal owing to the lack of work hardening, which results in negligible increase in the stress with respect to the increased strains, and therefore the comparable ultimate tensile strength values. However, the uniform elongation is significantly lower for the porosity specimens, which can be due to the development of micro-cracks in the material at the vicinity of the pores that is constrained by the surrounding material at lower stress. The general lack of work hardening of this alloy also contributes to the much reduced elongation.

Table 2. Tensile test results.

Specimen	0.2% offset strength (MPa)	Ultimate tensile strength (MPa)	Uniform Elongation (%)
Reference	802 ±7	859 ±4	10 ±2

Porosity	825 ±5	842 ±8	4 ±1

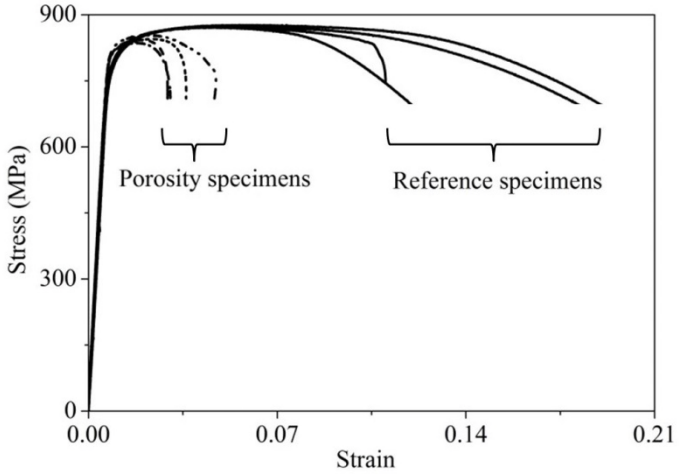

Fig. 6 Engineering stress vs. strain relations from tensile testing of the reference (solid lines) and porosity specimens (dotted lines).

The tensile fracture surfaces of a reference specimen and porosity specimen are shown in Figs. 7(a) and 7(b) respectively. Dimples are observed in both cases as shown by enlarged views in Figs. 7(c) and 7(d), thereby indicating a ductile fracture. However, the dimple sizes in the reference specimens (Fig. 7c) are significantly smaller than those in the porosity specimens (Fig. 7d). The smaller dimple size in the reference specimens can be due to the higher elongation that deforms (pulls) the grains resulting in the ruptured grains (manifested as dimples) having smaller cross-section at final fracture, whereas the porosity specimens undergo lower elongation and the grains are not deformed as much, and therefore the dimples are comparatively larger [50].

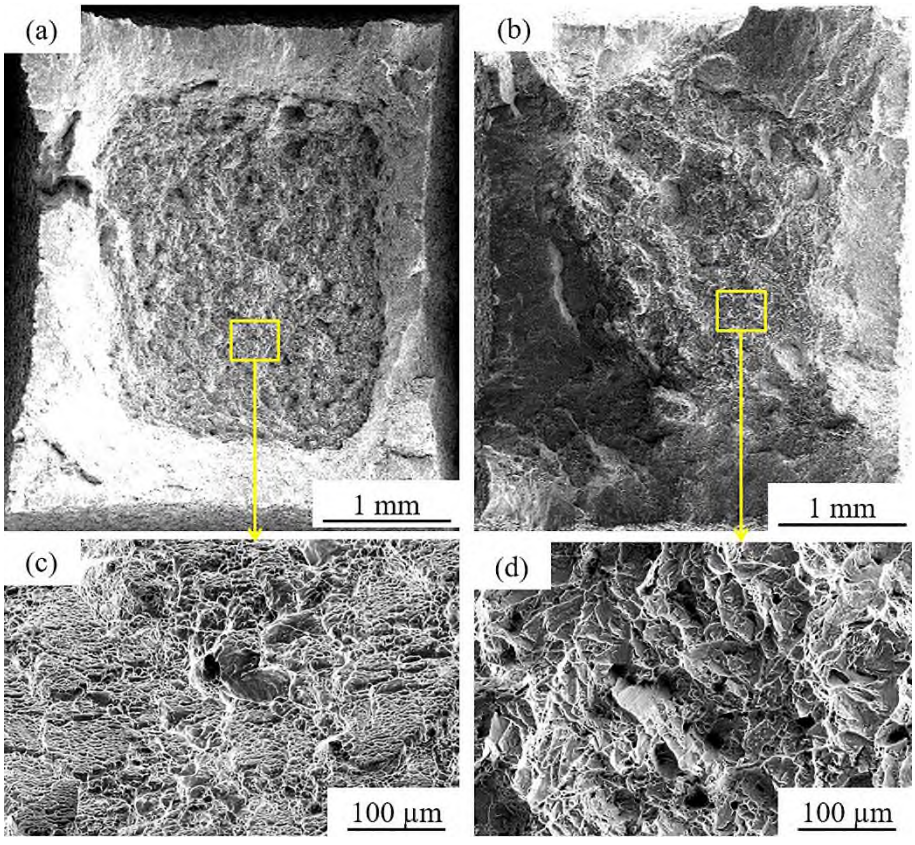

Fig. 7 Tensile fracture surfaces, (a) reference, (b) porosity, (c) and (d) enlarged views of (a) and (b) showing the dimple size differences.

3.4 Fatigue test results

It is known that in the high cycle fatigue regime, the total life of a coupon specimen is dominated by the crack initiation life, whereas in the low cycle fatigue regime, micro-cracks nucleate within a few tens or hundreds of loading cycles due to the higher applied stress levels, and therefore the total life is dominated by the crack propagation phase. Fig. 8 shows the fatigue test results obtained from the reference and porosity specimens. It was found that the scatter in the porosity specimen tests was significantly reduced for applied stress amplitudes of 270 MPa and above. The reason for this behaviour can be the local yielding at the pore vicinity leading to micro-crack nucleation within a few tens of loading cycles. Following this, the pore and the micro-crack collectively contribute to the crack propagation. Given the stress concentration factor of 2 in the porosity specimens, an applied stress amplitude of 270 MPa at stress ratio 0.1 is high enough to cause the crack to grow unhindered, leading to reduced scatter in the fatigue life. However, in the reference specimens, the micron sized pores coupled with the micro-crack, tend to remain within the size scale of the surrounding microstructure, thereby leading to an extended phase of short crack propagation. This phase has significant variation and scatters in the fatigue life owing to the microstructural interactions, e.g. the micro-crack deflects from grain to grain while seeking the easiest slip planes.

Fracture surface examination was performed to elucidate the differences among the three distinct S-N curves (Fig. 8); the S-N behaviour depends on whether the crack was initiated at microstructural features (no pores), at porosity of diameter comparable to the α colony width (pore diameters below 100 μm), or at porosity of diameter much larger than the α colony width (pore diameters above 100 μm). Compared to the defect-free reference specimens, the fatigue strength of porosity specimens was reduced by a factor of 1.5 (at 10^7 cycles). The best-fit curves were expressed using a power law relationship as shown in Eq. (1). The values of the two material constants (σ_f', b) were (827±47, −0.068±0.004) for the defect-free reference specimens, (818±60, −0.075±0.005) for those reference specimens with crack initiation at pores below 100 μm diameter, and (899±142, −0.107±0.01) for the porosity specimens with crack initiation at pores greater than 100 μm diameter.

$$\sigma_a = \sigma'_f (N)^b \quad (1)$$

where σ_a is the applied stress amplitude, σ'_f the fatigue strength coefficient, b the fatigue strength exponent, and N the load cycles to failure. Note that the material constant values are only valid for applied stress ratio of 0.1.

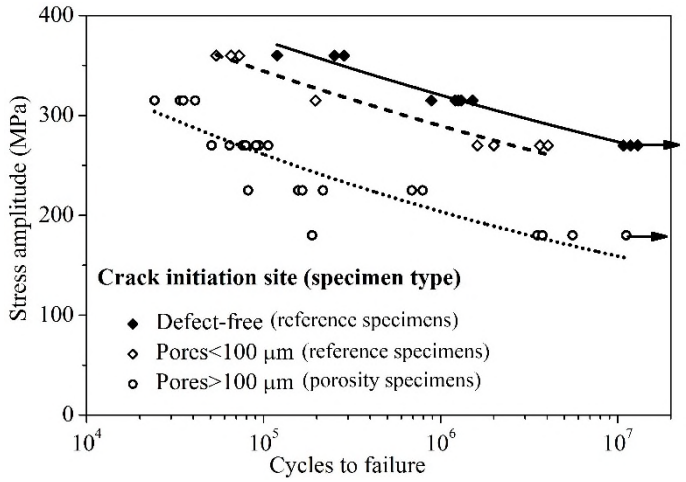

Fig. 8 Fatigue test results with information from fractography analysis. Three distinct S-N curves were identified depending on the crack initiation site and pore size. Note: the defect-free and micron sized pores (below 100 μm) specimens were extracted from the reference wall, representing the two extremes of material intrinsic behaviour. Lines indicate the best fit curves.

Fig. 9 shows the fracture surface of two specimens tested at the same load level. Measured diameter of the crack initiating pore in Fig. 9 (a-c) was comparable to the microstructure size, whereas the crack initiating pore diameter in Fig. 9 (d-f) was significantly larger than the microstructure size. Depending on the porosity size, the crack initiation and early stage growth manifested transgranular cleavage as shown in Fig. 9 (c) for the specimen with smaller porosity (dia. < 100 μm), whereas, the specimen with larger porosity (dia. > 200 μm) exhibited intergranular facets for as shown in Fig. 9 (f). Therefore, the higher fatigue life for the specimen with porosity size comparable to the microstructure characteristic length (i.e. width of lamellar α colony [46]) was due to the interaction of the pore with the microstructure. It is worth mentioning that the specimen with smaller porosity was from the reference group while the larger porosity specimen was from porosity group.

Fatigue life was found to be the lowest when multiple pores were present within a distance less than the diameter of the larger pore as shown in Fig. 10 (a). Proximity of the pore to the free surface was found to be the next most influential factor. Sub-surface location (Fig. 10b) has reduced the fatigue life by a factor of four as compared to the internal location (Fig. 10c). Additionally, it was observed that five specimens had crack initiation from surface defects, 18 at sub-surface defects, five at internal defects, and the remaining at microstructural features (defect-free). Therefore, sub-surface pore location was found to be the most critical case, as approximately 65% of the specimens had cracks initiated from subsurface pores.

Fig. 11 presents the results for the crack initiating pore diameter vs. fatigue life. It can be observed that the pores in the reference specimens were below 100 μm in diameter. However, the scatter in the results indicates that in addition to porosity size, the applied stress level should also be considered.

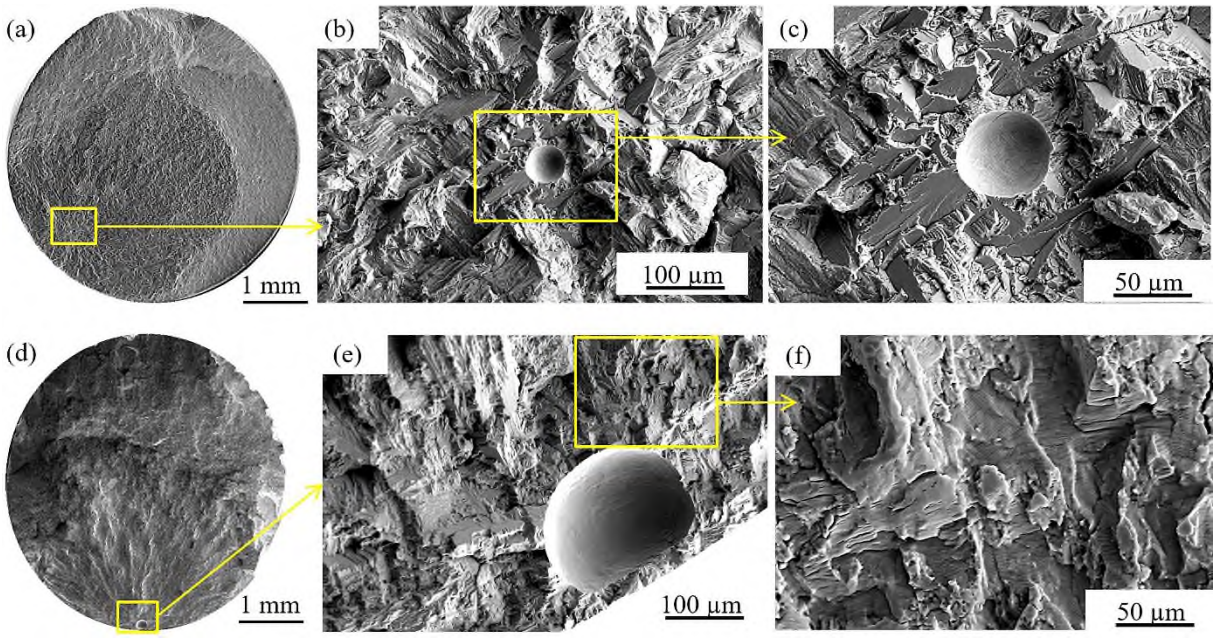

Fig. 9 Effect of porosity diameter on fatigue fracture behaviour; (a) - (c) initial porosity diameter (d_0 = 58 µm) is comparable to surrounding α colony size, $N = 8.8\times10^5$ cycles, (d) – (f) initial porosity diameter (d_0 = 220 µm) is much larger than surrounding α colony size, $N = 3.3\times10^4$ cycles. Both specimens were tested at applied stress amplitude of 315 MPa, stress ratio 0.1.

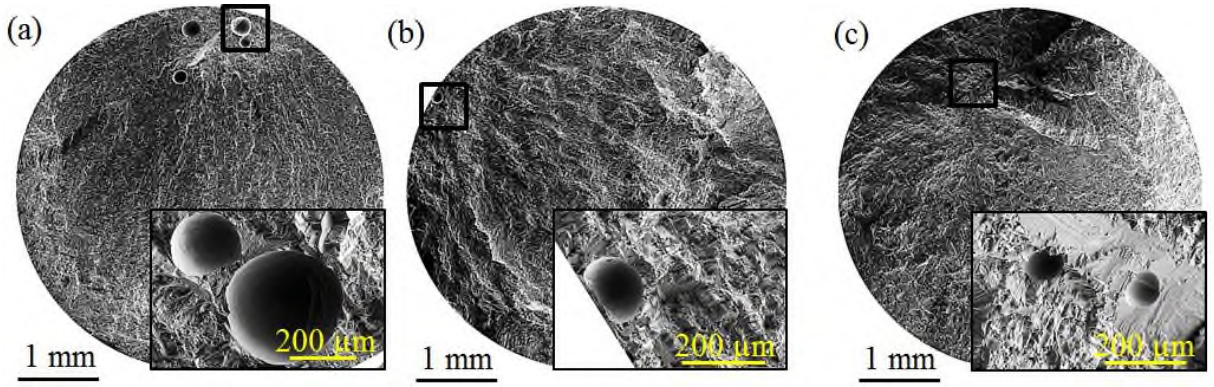

Fig. 10 Overall fracture surface with magnified view (bottom right corner) of the crack initiation site: (a) multiple pores at close proximity, d_0 = 320 µm, 197 µm, $N = 1.87\times10^5$ cycles, (b) sub-surface pore, d_0 = 190 µm, $N = 1.19\times10^6$ cycles, (c) internal pore, d_0 = 113 µm, 93 µm, $N = 5.57\times10^6$ cycles. All three specimens were tested at applied stress amplitude 180 MPa, stress ratio 0.1.

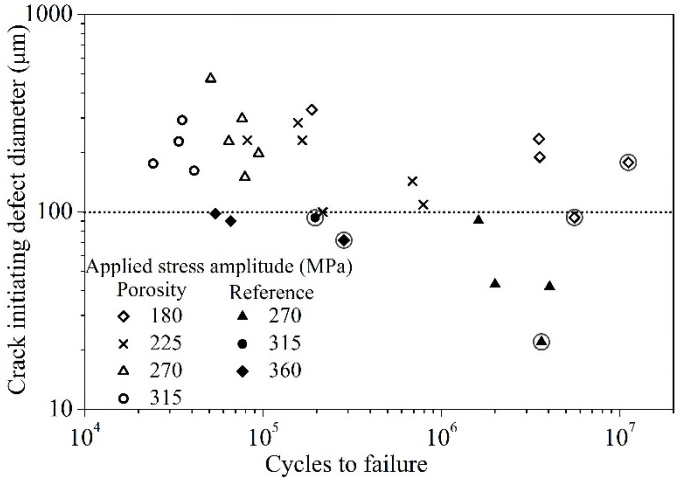

Fig. 11 Crack initiating pore diameter vs. fatigue life for the reference and porosity specimens showing no correlation between the defect size (pore diameter) and the fatigue life under various applied stress amplitudes. Note: encircled data points denote crack initiation at internal pores.

4 Fracture mechanics applied to gas pores

4.1 Stress intensity factor as a fatigue design parameter

When considered separately, neither the applied stress (Fig. 8) nor the crack initiating pore size (Fig. 11) could provide good correlation with the fatigue life. Therefore, fracture mechanics approach was applied for the test data correlation. According to Murakami's approach [28], a spherical gas pore can be treated as a planar crack of size equal to the square root of the projected area of the pore. Stress intensity factor range can be calculated by Murakami's equation as shown in Eq. (2).

$$\Delta K = C \times \Delta\sigma \sqrt{\pi \sqrt{area}} \tag{2}$$

where ΔK is the stress intensity factor (SIF) range, $\Delta\sigma$ the applied stress range, $\sqrt{area}$ the square root of the projected area of the pore, and parameter C is 0.5 for internal defects and 0.65 for surface defects [28].

Fatigue test result presented in Fig. 8 is now re-plotted as the relation of ΔK vs. N in Fig. 12 showing a much better correlation between the fatigue life and the fracture mechanics parameter. It is also observed that the best fit curve for the test data is kinked at around the value of threshold stress intensity factor range of the material (ΔK_{th}). The reason is that when the crack growth driving force, ΔK, is below its threshold value ΔK_{th}, crack growth rate is dropped exponentially, resulting in much increased fatigue life, hence the change in the slope of the best fit curves [51]. From Fig. 12, the threshold stress intensity factor range of the material was estimated as 4.5 MPa√m at the kinking point, which agrees with the values reported in literature for AM Ti-6Al-4V [6,9,13,52].

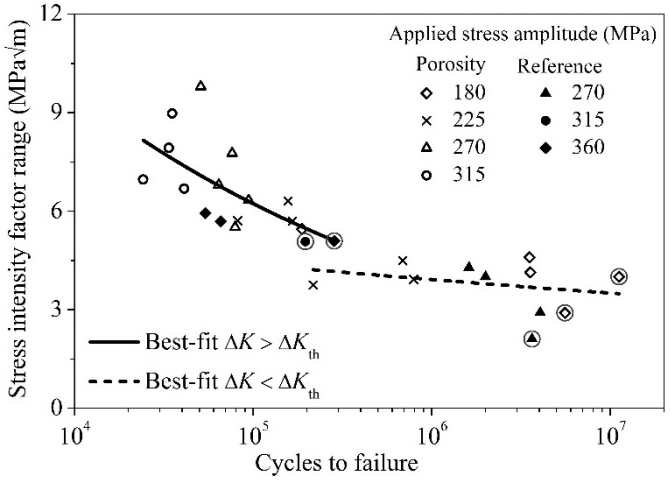

Fig. 12 Correlation between fatigue life and stress intensity factor range (SIF range) for porosity defects tested in this study (SIF range is calculated using the Murakami's equation, Eq. 2). Note: encircled data points denote crack initiation at internal pores.

4.2 Modified Kitagawa-Takahashi diagram

The original Kitagawa-Takahashi diagram (K-T diagram) combines the material's intrinsic fatigue limit and the LEFM non-propagating crack condition to set the fatigue limits [36]. It was developed

based on the LEFM material properties for long cracks. For defects, Beretta and Romano adapted and modified the K-T diagram [30]. However, a lower bound should be set for the K-T diagram by the notch fatigue limit for porosity defects. Therefore, in this study it is proposed that the K-T diagram for porosity defects should have three regions as shown in Fig. 13 and elaborated as follows.

(a) Region I is the upper bound of the fatigue limit and is set by the material's intrinsic fatigue limit. It is applicable when the porosity size is reduced to near zero, hence has negligible effect on the material's fatigue limit.

(b) Region II sets the criterion for non-propagating defects based on the LEFM condition of SIF range equal to the threshold SIF range (ΔK=ΔK_{th}).

(c) Region III is the lower bound of the fatigue limit curve and is set by the notch fatigue limit due to the defect. A previous study has applied this approach to modify the K-T diagram for notched specimens [53,54].

However, porosity size ranges only a few hundred microns and falls within the short crack regime. Since such defects propagate faster than long cracks at similar nominal SIF range [38,55], the LEFM condition would be non-conservative for porosity defects. Therefore, as presented in a previous study on defect tolerances [30], the porosity size was represented using Murakami's square root area argument and was applied in the El Haddad's model [29] to satisfy the similitude condition for porosity defects.

El Haddad et al. [29] introduced a fictitious crack length, a_0, as shown in Eq. (3) to apply the LEFM theory for short cracks. It is referred to as the El Haddad material constant, determined by Eq. (4). The El Haddad material constant increases the value of the SIF for short crack length.

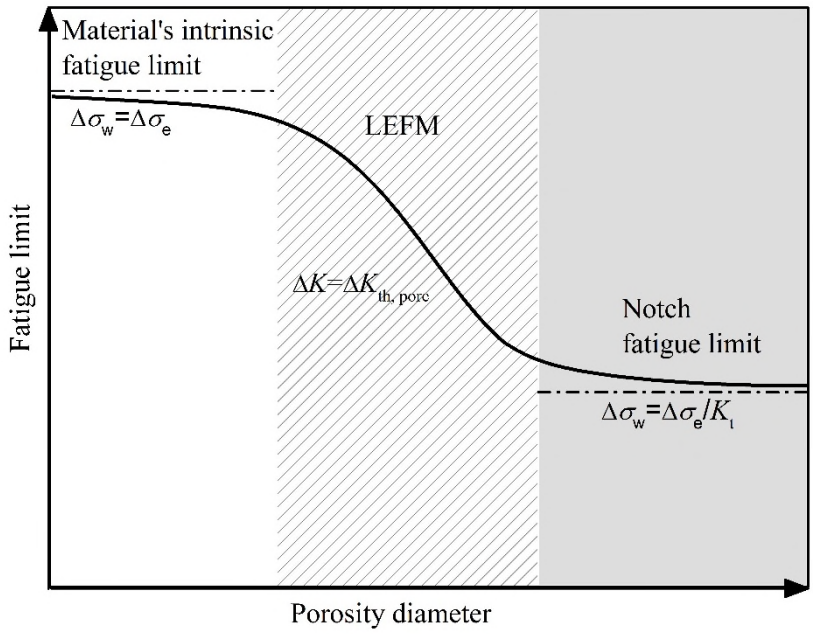

Fig. 13 Schematic of the proposed Kitagawa-Takahashi diagram for the effect of porosity size on the fatigue limit.

$$\Delta K = \Delta\sigma\sqrt{\pi(a + a_0)} \tag{3}$$

$$\Delta K_{\mathrm{th}} = \Delta\sigma_{\mathrm{e}}\sqrt{\pi a_0} \tag{4}$$

where ΔK is the stress intensity factor range, $\Delta\sigma$ the applied stress range, a the short crack length, a_0 the El Haddad material constant, ΔK_{th} the stress intensity factor range threshold obtained from long crack fatigue test (~4.5 MPa√m), $\Delta\sigma_e$ the intrinsic fatigue limit of the material (540 MPa for WAAM Ti-6Al-4V, R=0.1).

Let $\Delta K=\Delta K_{th}$, from Eqs. (3) and (4), the reduced fatigue limit, $\Delta\sigma_w$, is given by Eq. (5), which also bridges the fatigue limit to the linear elastic fracture mechanics threshold condition via a smooth transition region.

$$\Delta\sigma_w = \Delta\sigma_e \sqrt{\frac{a_0}{a_0 + a}} \tag{5}$$

where $\Delta\sigma_w$ is the reduced fatigue limit of the material due to short crack.

Beretta and Romano modified the El Haddad's model for porosity defects by replacing the short crack length in Eq. (5) with the Murakami's square root area parameter as shown in Eq. (6) [30] for calculating the fatigue limit for specimens with crack initiation at porosity defects. Further, Eq. (6) converges to the upper bound set by the material's intrinsic fatigue limit when the defect size reduces to zero (√area=0).

$$\Delta\sigma_w = \Delta\sigma_e \sqrt{\frac{\sqrt{area_0}}{\sqrt{area} + \sqrt{area_0}}} \tag{6}$$

where √area is the defect size expressed according to Murakami's square root area argument, and $\sqrt{area}_0$ is the modified El Haddad parameter that was calculated according to Eq. (2) by replacing ΔK with $\Delta K_{th,LC}$ (4.5 MPa√m) and $\Delta\sigma$ with the material's intrinsic fatigue limit $\Delta\sigma_e$ (540 MPa). Therefore, the El Haddad parameter in Eq. (6) for WAAM Ti-6Al-4V was calculated as 52 μm for both surface and sub-surface pores, and 88 μm for internal pores.

The lower bound was determined from Eq. (7). However, use of stress concentration factor can be conservative as the notch sensitivity of Ti-6Al-4V is often reported to be between 0.5 to 0.6 [56,57]. Therefore, Eq. (8) was used to find the notch fatigue factor, K_f, which sets the lower bound of the K-T diagram for porosity defects.

$$\Delta\sigma_w = \frac{\Delta\sigma_e}{K_t} \tag{7}$$

$$\Delta\sigma_w = \frac{\Delta\sigma_e}{K_f} \tag{8}$$

where K_t is the stress concentration factor and the value for spherical internal pores is 2.08 [25]. K_f is the notch fatigue factor determined by the ratio of the fatigue limit of the reference (or smooth) specimens to the fatigue limit of the porosity specimens. The value of K_f was 1.5 for the fatigue test results presented in this study (Fig. 8).

The modified K-T diagram for porosity defects with the three limiting conditions (material's intrinsic fatigue limit as upper bound, modified El Haddad's LEFM criterion, and the notch fatigue limit as the lower bound) was found to agree well with the test results as shown in Fig. 14.

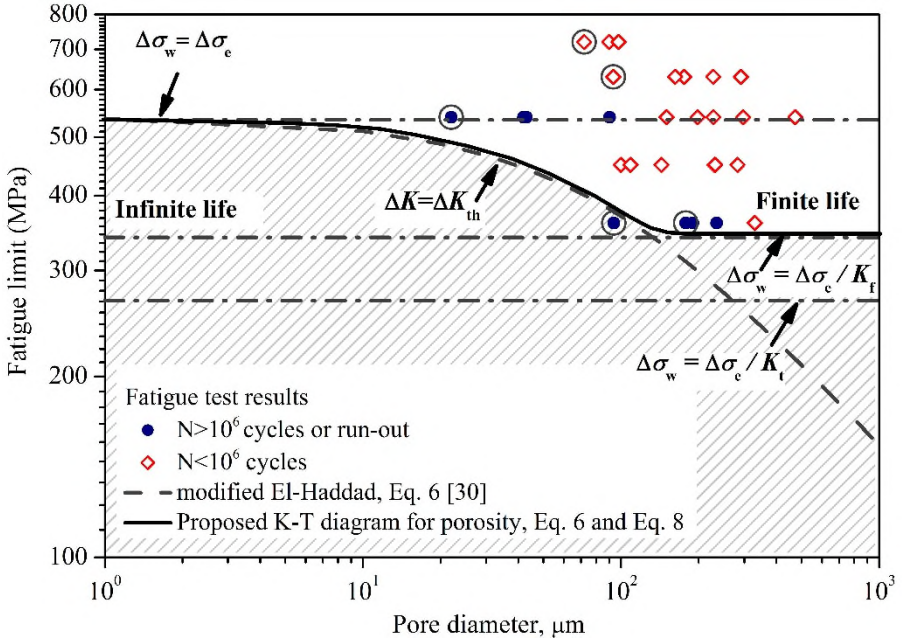

Fig. 14 Calculated fatigue strength limit (solid line) for WAAM Ti-6Al-4V as a function of porosity diameter. Material's intrinsic fatigue limit ($\Delta\sigma_e$) is 540 MPa at applied stress ratio 0.1. Note: encircled data points denote crack initiation at internal pores. Test results are from this study (Section 3.4).

5 Conclusions

Two groups of specimens were made by the wire + arc additive manufactured titanium alloy (WAAM Ti-6Al-4V) and tested to study the material performance of the reference group (manufactured with clean wire) and porosity group (manufactured with contaminated wire at the specimen gauge section). The study has included microstructure analysis, porosity characterization, fatigue testing and fracture mechanics analysis. Following conclusions can be drawn:

1. The microstructure of both groups was similar and consisted of epitaxial prior β grains aligned along the material build direction. The α phase exhibited the Widmanstätten and lamellar colony morphology with an average α lath width of 3 μm and α colony width of 20-30 μm. Average gas pore diameter was 60 μm for the reference group and 200 μm for the porosity group.

2. Fatigue strength in terms of the maximum applied stress at 10 million cycles, at stress ratio 0.1, was 600 MPa and 400 MPa, respectively, for the reference and porosity specimens. The static tensile strength properties were comparable for the two specimen groups, but the uniform elongation was very different, at 10% (reference) and 4% (porosity specimens).

3. Fatigue life can be correlated with the stress intensity factor range of the crack initiating defect using Murakami's equation, which takes account of both the applied stress level and defect size. The best fit line of the correlation is kinked at the point (or value) corresponding to the threshold stress intensity factor range.

4. Fatigue strength limit can be predicted by a modified Kitagawa-Takahashi diagram for porosity defects Instead of using a monotonically decreasing relation of the applied stress range with porosity size, a sigmoidal curve is used in this study to set the lower bound according to the notch fatigue limit. The critical porosity diameter was found to be close to 100 μm for WAAM Ti-6Al-4V.

Acknowledgements

We are grateful to Coventry University for the PhD studentship to Romali Biswal. We also thank Dr. Filomeno Martina for providing the chemical composition of the test materials.

References

[1] Martina F, Mehnen J, Williams SW, Colegrove P, Wang F. Investigation of the benefits of plasma deposition for the additive layer manufacture of Ti-6Al-4V. J Mater Process Technol 2012;212:1377–86. doi:10.1016/j.jmatprotec.2012.02.002.

[2] Cunningham CR, Flynn JM, Shokrani a., Dhokia V, Newman ST. Invited review article: Strategies and processes for high quality wire arc additive manufacturing. Addit Manuf 2018;22:672–86. doi:10.1016/j.addma.2018.06.020.

[3] Hönnige JR, Colegrove PA, Ahmad B, Fitzpatrick ME, Ganguly S, Lee TL, et al. Residual stress and texture control in Ti-6Al-4V wire + arc additively manufactured intersections by stress relief and rolling. Mater Des 2018;150:193–205. doi:10.1016/j.matdes.2018.03.065.

[4] Zhang X, Martina F, Ding J, Wang X, Williams SW. Fracture toughness and fatigue crack growth rate properties in wire + arc additive manufactured Ti-6Al-4V. Fatigue Fract Eng Mater Struct 2017;40:790–803. doi:10.1111/ffe.12547.

[5] Wang F, Williams S, Colegrove PA, Antonysamy AA. Microstructure and mechanical properties of wire and arc additive manufactured Ti-6Al-4V. Metall Mater Trans A Phys Metall Mater Sci 2013;44:968–77. doi:10.1007/s11661-012-1444-6.

[6] Leuders S, Thöne M, Riemer A, Niendorf T, Tröster T, Richard HA, et al. On the mechanical behaviour of titanium alloy TiAl6V4 manufactured by selective laser melting: Fatigue resistance and crack growth performance. Int J Fatigue 2013;48:300–7. doi:10.1016/j.ijfatigue.2012.11.011.

[7] Edwards P, O'Conner A, Ramulu M. Electron Beam Additive Manufacturing of Titanium Components: Properties and Performance. J Manuf Sci Eng 2013;135:061016. doi:10.1016/0168-9002(88)90649-3.

[8] Tammas-Williams S, Withers PJ, Todd I, Prangnell PB. The influence of porosity on fatigue crack initiation in additively manufactured titanium components. Sci Rep 2017:1–13. doi:10.1038/s41598-017-06504-5.

[9] Wycisk E, Solbach A, Siddique S, Herzog D, Walther F, Emmelmann C. Effects of defects in laser additive manufactured Ti-6Al-4V on fatigue properties. Phys Procedia 2014;56:371–8. doi:10.1016/j.phpro.2014.08.120.

[10] Wan H, Wang Q, Jia C, Zhang Z. Multi-scale damage mechanics method for fatigue life prediction of additive manufacture structures of Ti-6Al-4V. Mater Sci Eng A 2016;669:269–78. doi:10.1016/j.msea.2016.05.073.

[11] Kasperovich G, Hausmann J. Improvement of fatigue resistance and ductility of TiAl6V4 processed by selective laser melting. J Mater Process Technol 2015;220:202–14. doi:10.1016/j.jmatprotec.2015.01.025.

[12] Martina F, Colegrove PA, Williams SW, Meyer J. Microstructure of interpass rolled wire + arc additive manufacturing Ti-6Al-4V components. Metall Mater Trans A Phys Metall Mater Sci 2015;46:6103–18. doi:10.1007/s11661-015-3172-1.

[13] Antonysamy AA. Microstructure , texture and mechanical property evolution during additive manufacturing of Ti6Al4V alloy for aerospace applications, PhD thesis, Manchester university, UK. 2012.

[14] Lin JJ, Lv YH, Liu YX, Xu BS, Sun Z, Li ZG, et al. Microstructural evolution and mechanical properties of Ti-6Al-4V wall deposited by pulsed plasma arc additive manufacturing 2016;102:30–40. doi:10.1016/j.matdes.2016.04.018.

[15] Bermingham MJ, Kent D, Zhan H, Stjohn DH, Dargusch MS. Controlling the microstructure and properties of wire arc additive manufactured Ti-6Al-4V with trace boron additions. Acta Mater 2015;91:289–303. doi:10.1016/j.actamat.2015.03.035.

[16] Wire+Arc Additive Manufacturing website 2018. https://waammat.com/documents.

[17] Baufeld B, Biest O Van Der, Gault R. Additive manufacturing of Ti–6Al–4V components by shaped metal deposition: Microstructure and mechanical properties. Mater Des 2010;31:S106–11. doi:10.1016/j.matdes.2009.11.032.

[18] Zhang H, Xie Y, Rui D, Wang G. Hybrid deposition and micro rolling manufacturing method of metallic parts. 24th Int SFF Symp - An Addit Manuf Conf SFF 2013 2013:267–81.

[19] Colegrove PA, Martina F, Roy MJ, Szost BA, Terzi S, Williams SW, et al. High Pressure Interpass Rolling of Wire + Arc Additively Manufactured Titanium Components. Adv Mater Res 2014;996:694–700. doi:10.4028/www.scientific.net/AMR.996.694.

[20] McAndrew AR, Alvarez Rosales M, Colegrove PA, Hönnige JR, Ho A, Fayolle R, et al. Interpass rolling of Ti-6Al-4V wire + arc additively manufactured features for microstructural refinement. Addit Manuf 2018;21:340–9. doi:10.1016/j.addma.2018.03.006.

[21] Qvale P, Härkegård G. A simplified method for weakest-link fatigue assessment based on finite element analysis. Int J Fatigue 2017;100:78–83. doi:10.1016/j.ijfatigue.2017.03.010.

[22] Siddique S, Awd M, Tenkamp J, Walther F. Development of a stochastic approach for fatigue life prediction of AlSi12 alloy processed by selective laser melting. Eng Fail Anal 2017;79:34–50. doi:10.1016/j.engfailanal.2017.03.015.

[23] Romano S, Brandão a., Gumpinger J, Gschweitl M, Beretta S. Qualification of AM parts: Extreme value statistics applied to tomographic measurements. Mater Des 2017;131:32–48. doi:10.1016/j.matdes.2017.05.091.

[24] Beretta S, Chai G, Soffiati E. A weakest–link analysis for fatigue strength of components containing defects. Convegno IGF XVII Bol. 2004, 2008.

[25] Biswal R, Syed AK, Zhang X. Assessment of the effect of isolated porosity defects on the fatigue performance of additive manufactured titanium alloy. Addit Manuf 2018;23:433–42. doi:10.1016/j.addma.2018.08.024.

[26] Härkegård G. Short-crack modelling of the effect of corrosion pits on the fatigue limit of 12% Cr steel. Fatigue Fract Eng Mater Struct 2015;38:1009–16. doi:10.1111/ffe.12305.

[27] Härkegrd G, Halleraker G. Assessment of methods for prediction of notch and size effects at the fatigue limit based on test data by Böhm and Magin. Int J Fatigue 2010;32:1701–9. doi:10.1016/j.ijfatigue.2010.03.011.

[28] Murakami Y. Metal fatigue: Effects of Small Defects and Nonmetallic Inclusions. 1st ed. Elsevier; 2002.

[29] El Haddad MH, Topper TH, Smith KN. Prediction of non propagating cracks. Eng Fract Mech 1979;11:573–84.

[30] Beretta S, Romano S. A comparison of fatigue strength sensitivity to defects for materials manufactured by AM or traditional processes. Int J Fatigue 2017;94:178–91. doi:10.1016/j.ijfatigue.2016.06.020.

[31] Hiroshige Masuo, Yuzo Tanaka, Shotaro Morokoshi, Hajime Yagura, Tetsuya Uchida, Yasuhiro Yamamoto YM. Effects of Defects , Surface Roughness and HIP on Fatigue of Ti-6Al-4V manufactured by Additive Manufacturing. Procedia Struct Integr 2017;7:19–26. doi:10.1016/j.prostr.2017.11.055.

[32] Romano S, Brückner-Foit a., Brandão a., Gumpinger J, Ghidini T, Beretta S. Fatigue properties of AlSi10Mg obtained by additive manufacturing: Defect-based modelling and prediction of fatigue strength. Eng Fract Mech 2018;187:165–89. doi:10.1016/j.engfracmech.2017.11.002.

[33] Yamashita Y, Murakami T, Mihara R, Okada M, Murakami Y. Defect analysis and fatigue design basis for Ni-based superalloy 718 manufactured by selective laser melting. Int J Fatigue 2018;117:485–95.

doi:10.1016/j.ijfatigue.2018.08.002.

[34] Bermingham MJ, Nicastro L, Kent D, Chen Y, Dargusch MS. Optimising the mechanical properties of Ti-6Al-4V components produced by wire þ arc additive manufacturing with post-process heat treatments. J Alloys Compd 2018;753:247–55. doi:10.1016/j.jallcom.2018.04.158.

[35] Erhard Brandl, Christoph Leyens FP. Mechanical Properties of Additive Manufactured Ti-6Al-4V Using Wire and Powder Based Processes. IOP Conf Ser Mater Sci Eng 2011;26. doi:10.1088/1757-899X/26/1/012004.

[36] Kitagawa H, Takahashi S. Applicability of fracture mechanics to very small cracks or the cracks in the early stage. Proc 2nd Int conf mech Behav. mater - ICM2, 1976, p. 627–31.

[37] Broek D. Elementary Engineering Fracture Mechanics. 3rd ed. Martinus Nijhoff; 1982.

[38] Pearson S. Initiation of fatigue cracks in commercial aluminium alloys and the subsequent propagation of very short cracks. Eng Fract Mech 1975;7. doi:10.1016/0013-7944(75)90004-1.

[39] Murakami Y, Endo M. Effects of Hardness and Crack Geometries on DeltaKth of Small Cracks Emanating from Small Defects. Mechanical Engineering Publications; 1986.

[40] Greitemeier D, Palm F, Syassen F, Melz T. Fatigue performance of additive manufactured TiAl6V4 using electron and laser beam melting. Int J Fatigue 2016;44:211–7. doi:10.1016/j.ijfatigue.2016.05.001.

[41] Leuders S, Vollmer M, Brenne F, Tröster T, Niendorf T. Fatigue strength prediction for titanium alloy TiAl6V4 manufactured by selective laser melting. Metall Mater Trans A 2015;46:3816–23. doi:10.1007/s11661-015-2864-x.

[42] ASTM International. ASTM F3302-18, Standard for Additive Manufacturing – Finished Part Properties – Standard Specification for Titanium Alloys via Powder Bed Fusion 2018:8. doi:10.1520/F3302-18.

[43] ASTM Int. Standard guide for preparation of metallographic specimens. Astm 2017;E3-11:1–17. doi:10.1520/E0003-11R17.

[44] ASTM Int. Standard test methods for tension testing of metallic materials. Astm 2015;E8-15:1–27. doi:10.1520/E0008_E0008M-15A.

[45] Shi R, Dixit V, Fraser HL, Wang Y. Variant selection of grain boundary α by special prior β grain boundaries in titanium alloys. Acta Mater 2014;75:156–66. doi:10.1016/j.actamat.2014.05.003.

[46] Chan KS. Roles of microstructure in fatigue crack initiation. Int J Fatigue 2010;32:1428–47. doi:10.1016/j.ijfatigue.2009.10.005.

[47] Lutjering G, Williams J. Engineering Materials and Processes - Titanium. 2nd ed. 2007.

[48] Tammas-Williams S, Zhao H, Léonard F, Derguti F, Todd I, Prangnell PB. XCT analysis of the influence of melt strategies on defect population in Ti–6Al–4V components manufactured by Selective Electron Beam Melting. Mater Charact 2015;102:47–61. doi:10.1016/j.matchar.2015.02.008.

[49] Siddique S, Imran M, Rauer M, Kaloudis M, Wycisk E, Emmelmann C, et al. Computed tomography for characterization of fatigue performance of selective laser melted parts. Mater Des 2015;83:661–9. doi:10.1016/j.matdes.2015.06.063.

[50] Das A, Tarafder S. Geometry of dimples and its correlation with mechanical properties in austenitic stainless steel. Scr Mater 2008;59:1014–7. doi:10.1016/j.scriptamat.2008.07.012.

[51] Benedetti M, Fontanari V. The effect of bi-modal and lamellar microstructures of Ti-6Al-4V on the behaviour of fatigue cracks emanating from edge-notches. Fatigue Fract Eng Mater Struct 2004;27:1073–89. doi:10.1111/j.1460-2695.2004.00825.x.

[52] Seifi M, Dahar M, Harrysson O, Beuth J, Lewandowski JJ. Evaluation of Orientation Dependence of Fracture Toughness and Fatigue Crack Growth Behavior of as-deposited ARCAM EBM Ti-6Al- 4V 2015. doi:10.1007/s11837-015-1298-7.

[53] Atzori B, Lazzarin P, Meneghetti G. Fracture mechanics and notch sensitivity. Fatigue Fract Eng Mater Struct 2003;26:257–67. doi:10.1046/j.1460-2695.2003.00633.x.

[54] Atzori B, Lazzarin P, Meneghetti G. A unified treatment of the mode i fatigue limit of components containing notches or defects. Int J Fract 2005;133:61–87. doi:10.1007/s10704-005-2183-0.

[55] Suresh S, Ritchie RO. Propagation of short fatigue cracks. Int Met Rev 1984;29:445–75. doi:10.1179/imtr.1984.29.1.445.

[56] Kahlin M, Ansell H, Moverare JJ. Fatigue behaviour of notched additive manufactured Ti6Al4V with as-built surfaces. Int J Fatigue 2017;101:51–60. doi:10.1016/j.ijfatigue.2017.04.009.

[57] Razavi SMJ, Berto F. ScienceDirect Fatigue strength of notched specimens made of Ti-6Al-4V produced by SLM technique. Procedia Struct Integr 2018;00:0–4. doi:10.1016/j.prostr.2018.12.013.

https://dspace.org/

Criticality of porosity defects on the fatigue performance of wire+arc additive manufactured titanium alloy

Biswal, Romali; Zhang, Xiang; Syed, Abdul Khadar; Awd, Mustafa; Ding, Jialuo ...

2019-01-28
Elsevier
https://doi.org/10.1016/j.ijfatigue.2019.01.017
Biswal R, Zhang X, Syed A, et al., Criticality of porosity defects on the fatigue performance of wire+arc additive manufactured titanium alloy. International Journal of Fatigue, Volume 122, May 2019, pp. 208-217

Downloaded from a DSpace repository. https://dspace.org/